

GENERATION OF HIGH-FREQUENCY P AND S WAVE ENERGY BY ROCK FRACTURE DURING A BURIED EXPLOSION

Charles G. Sammis and Ares J. Rosakis

**University of Southern California
Department of Earth Sciences
Los Angeles, CA 90089-0740**

20 July 2015

Final Report

APPROVED FOR PUBLIC RELEASE; DISTRIBUTION IS UNLIMITED.



**AIR FORCE RESEARCH LABORATORY
Space Vehicles Directorate
3550 Aberdeen Ave SE
AIR FORCE MATERIEL COMMAND
KIRTLAND AIR FORCE BASE, NM 87117-5776**

DTIC COPY

NOTICE AND SIGNATURE PAGE

Using Government drawings, specifications, or other data included in this document for any purpose other than Government procurement does not in any way obligate the U.S. Government. The fact that the Government formulated or supplied the drawings, specifications, or other data does not license the holder or any other person or corporation; or convey any rights or permission to manufacture, use, or sell any patented invention that may relate to them.

This report was cleared for public release by the 377 ABW Public Affairs Office and is available to the general public, including foreign nationals. Copies may be obtained from the Defense Technical Information Center (DTIC) (<http://www.dtic.mil>).

AFRL-RV-PS-TR-2015-0145 HAS BEEN REVIEWED AND IS APPROVED FOR PUBLICATION IN ACCORDANCE WITH ASSIGNED DISTRIBUTION STATEMENT.

//SIGNED//

Dr. Robert Raistrick
Project Manager, AFRL/RVBYE

//SIGNED//

Glenn M. Vaughan, Colonel, USAF
Chief, Battlespace Environment Division

This report is published in the interest of scientific and technical information exchange, and its publication does not constitute the Government's approval or disapproval of its ideas or findings.

REPORT DOCUMENTATION PAGE				Form Approved OMB No. 0704-0188	
Public reporting burden for this collection of information is estimated to average 1 hour per response, including the time for reviewing instructions, searching existing data sources, gathering and maintaining the data needed, and completing and reviewing this collection of information. Send comments regarding this burden estimate or any other aspect of this collection of information, including suggestions for reducing this burden to Department of Defense, Washington Headquarters Services, Directorate for Information Operations and Reports (0704-0188), 1215 Jefferson Davis Highway, Suite 1204, Arlington, VA 22202-4302. Respondents should be aware that notwithstanding any other provision of law, no person shall be subject to any penalty for failing to comply with a collection of information if it does not display a currently valid OMB control number. PLEASE DO NOT RETURN YOUR FORM TO THE ABOVE ADDRESS.					
1. REPORT DATE (DD-MM-YYYY) 20-7-2015		2. REPORT TYPE Final Report		3. DATES COVERED (From - To) 25 May 2012 – 09 Jul 215	
4. TITLE AND SUBTITLE Generation of High-Frequency P and S Wave Energy by Rock Fracture During a Buried Explosion				5a. CONTRACT NUMBER FA9453-12-C-0210	
				5b. GRANT NUMBER	
				5c. PROGRAM ELEMENT NUMBER 62601F	
6. AUTHOR(S) Charles G. Sammis and Ares J. Rosakis				5d. PROJECT NUMBER 1010	
				5e. TASK NUMBER PPM00014478	
				5f. WORK UNIT NUMBER EF007747	
7. PERFORMING ORGANIZATION NAME(S) AND ADDRESS(ES) University of Southern California Department of Earth Sciences Los Angeles, CA 90089-0740				8. PERFORMING ORGANIZATION REPORT NUMBER	
9. SPONSORING / MONITORING AGENCY NAME(S) AND ADDRESS(ES) Air Force Research Laboratory Space Vehicles Directorate 3550 Aberdeen Avenue SE Kirtland AFB, NM 87117-5776				10. SPONSOR/MONITOR'S ACRONYM(S) AFRL/RVBYE	
				11. SPONSOR/MONITOR'S REPORT NUMBER(S) AFRL-RV-PS-TR-2015-0145	
12. DISTRIBUTION / AVAILABILITY STATEMENT Approved for public release; distribution is unlimited. (377ABW-2015-0712 dtd 03 Sep 2015)					
13. SUPPLEMENTARY NOTES					
14. ABSTRACT We have developed a micromechanical damage mechanics model that is capable of predicting the nucleation, growth, and interaction of fracture damage at the high loading rates found in the non-linear source region of underground nuclear explosions. This model predicts the generation of strong S wave radiation in the non-linear source region whenever spherical symmetry is broken. Spherical symmetry is broken by the following: tectonic pre-stress, preferred orientation of pre-existing fractures (anisotropic rock fabric), and the lithostatic stress gradient. We are verifying this model by using it to predict the fracture patterns and S wave radiation generated by laboratory explosions in plates of "candy glass". Candy glass (or break-away glass) is used in the movie industry to simulate glass fracture in stunts with no injury to the actors. We have measured the elastic velocities, density, fracture toughness, and the size and density of initial flaws of this material as required input parameters to our model. We have also used laser velocimeters (as high speed seismometers) to measure the seismic radiation generated by these laboratory explosions. The dynamic damage mechanics model gives a good simulation of the fracture pattern and associated elastic radiation in these experiments. We have recently extended the damage model to allow an anisotropic distribution of initial damage and used it to model the asymmetric fracture pattern and seismic radiation observed for a chemical explosion in a granite quarry in Barre, Vermont.					
15. SUBJECT TERMS seismic source generation, explosion source physics, underground explosion, micromechanical damage mechanics					
16. SECURITY CLASSIFICATION OF:			17. LIMITATION OF ABSTRACT Unlimited	18. NUMBER OF PAGES 34	19a. NAME OF RESPONSIBLE PERSON Dr. Robert Raistrick
a. REPORT Unclassified	b. ABSTRACT Unclassified	c. THIS PAGE Unclassified			19b. TELEPHONE NUMBER (include area code)

This page is intentionally left blank

Table of Contents

1. Summary	1
2. Introduction.....	2
3. Methods, Assumptions, and Procedures	3
3.1. Numerical Modeling – Dynamic Damage Mechanics.....	3
3.2. Numerical Modeling – Anisotropic Initial Damage	3
3.3. Laboratory Experiments – Explosions in Candy-Glass Samples	8
4. Results and Discussion	9
4.1. Experimental Results – Candy-Glass Plates	9
4.2. Measurements of the Mechanical Properties of Candy-Glass	15
4.3 Numerical Simulations of Explosions	19
4.4 Effect of Burn-Rate (Loading Rate) on the Damage Pattern	21
4.5 Modeling an Anisotropic Initial Flaw Distribution	22
5. Conclusions.....	23
6. Recommendations.....	23
References	25

List of Figures

1. Isotropic damage generation in an explosion.....	4
2. Velocity anisotropy in Barre granite indicates a fracture anisotropy with microfractures preferentially aligned in the “rift plane”.....	4
3. Damage pattern produced by a NEDE explosion	5
4. Dynamic stresses in the near-field of an explosion.....	6
5. Explosion in granite that has a preferred fracture orientation (rift plane)	7
6. The initial damage state (D_0) of the model used to study an anisotropic solid.....	7
7. Experimental configuration used to produce fracture patterns in candy-glass	9
8. Photo of a sample before the explosion showing placement of the laser sensors	10
9. Image of the sample 20.0 μ s after the explosion	10
10. Image of the sample 60.0 μ s after the explosion	11
11. Image of the sample at the end of the experiment showing the fracture pattern.	11
12. Comparison of the experimental fracture pattern with that produced by an underground nuclear explosion.....	12
13. Recordings of the x component of velocity from experiment #1 recorded at the three stations indicated in Fig. 2.	12
14. Recordings of the x component of velocity from experiment #2, which used the same station configuration as experiment #1 as indicated in Fig. 2.	13
15. Travel paths for the arrivals plotted on travel time curves in Figs. 16 and 17.....	13
16. Travel time curves for experiment #1	14
17. Travel time curves from experiment #2.....	14
18. Locations of the ultrasonic measurements of V_p and V_s in a candy-glass plate.	15
19. Four point bending geometry used to measure the critical stress intensity factor K_{IC} in candy glass.....	16
20. Experimental geometry used to measure the uniaxial strength of candy-glass	18

21. Uniaxial stress-strain curves for candy glass used to determine a and D_0 as described in the text.	18
22. Comparison of simulated and measured velocity at sensor A in experiment #2	19
23. An identical simulation to that in Fig. 22 except that the critical stress intensity factor has been increased to the point where the explosion does no additional damage. ...	20
24. Radial velocity trace from a borehole seismometer 15 m from the NEDE chemical explosion in a Bare Granite quarry conducted by Weston Geophysical and New England Research.....	20
25. Simulation of the velocity traces in experiment #2.	21
26. Numerical simulations of point explosions in candy-glass plates showing the effect of the duration of loading T.	21
27. Numerical simulations of a point explosion in an anisotropic medium where the initial fractures have a preferential alignment in the rift direction.....	22
28. Numerical simulation of the P and S wave radiation from a point explosion in an anisotropic medium where the initial fractures have a preferential alignment in the rift direction, which is at 45° in this case.....	23

List of Tables

1. Elastic properties of candy-glass measured at New England Research.....	16
2. Specimen dimensions for the five test specimens.....	17
3. Test data and measured values of K_{IC} for the five test specimens	17

1. SUMMARY

The overall objective of this contract is to characterize and model the fracture damage produced in the non-linear source regime of an explosion and to understand its effect on the generation of seismic waves. We are particularly interested in the role of fracture damage in the generation of shear waves. Our approach has been a combination of numerical modeling and laboratory studies using high-speed digital photography.

During the first year we finished our modification of the micromechanical damage mechanics formulated by Ashby and Sammis [1990] and generalized by Deshpande and Evans [2008] to allow for a more generalized stress state and have incorporated an experimentally motivated new crack growth (damage evolution) law that is valid over a wide range of loading rates. This law is sensitive to both the crack tip stress field and its time derivative. Incorporating this feature produces strain-rate sensitivity in the constitutive response. This work was published in Bhat et al. [2012], which developed the model and showed how it was implemented as a user-defined subroutine in the ABAQUS dynamic finite element code. Bhat et al. [2012] also validated the model by reproducing the observed stress-strain behavior of Pentelicon marble over a 10 order of magnitude range of loading rates and used it in first order simulations of an underground explosion and an earthquake.

During the first year we also produced fracture patterns in the laboratory, photographed them using high-speed digital cameras, and monitored the resultant seismic waves using a laser vibrometer (as an ultra-high-frequency seismometer). We originally generated fracture patterns in the photoelastic polymer Homalite using hyper-velocity projectile impacts (impact velocity $> V_P$), but there was the troubling possibility that we were generating out-of-plane deformation that was affecting the pattern. Since the hyper-velocity experiments are performed in a vacuum chamber, applying a pre-stress to the plate and using laser velocimeters to monitor the elastic waves presented extreme experimental challenges.

A simpler experimental configuration was developed that used an exploding nichrome wire as a point pressure source to fracture the plate. However, our exploding wire did not produce enough energy to fracture the Homalite plates. We solved this problem by using “candy-glass”, the extremely brittle material used in bar fights in the movies. Our exploding wire produces excellent fracture patterns in this material. We have also used laser vibrometers to record particle velocities in the resultant P and S waves. Since no mechanical data was available for candy-glass, we measured V_P , V_S , and density, as well as the critical stress intensity factor K_{IC} . Although V_P and V_S are comparable to values in Homalite, K_{IC} is a factor of 67 times smaller, accounting for the extreme brittle behavior of candy-glass.

During the second year we ran two explosion experiments in candy glass plates photographing them using high-speed digital cameras, and monitoring the resultant seismic waves using laser vibrometers (as an array of ultra-high-frequency seismometers). We constructed travel-time curves, which we used to measure fracture damage near the source. We observed a double peak structure in the original pressure pulse and could demonstrate that the second pulse is caused by dilatation associated with fracture damage that develops behind the initial shock front. We also observed S waves on the transverse vibrometer in the near field.

During the second year we also ran a series of uniaxial compression tests to determine the size and density of initial flaws in candy-glass. These properties were used in conjunction with the elastic constants, density, and critical stress intensity factor as inputs in our dynamic

micromechanical damage mechanics in order to simulate the experiments. These simulations reproduced the structure of the fracture pattern, and most characteristics of the seismic radiation including the double initial peak and the shear wave in the near field. The experimental results in candy glass will soon be published [Mihaly et al., 2015].

During the third year we focused on the effects of fracture anisotropy and the free surface on the seismic radiation in general and the generation of S waves in specific. This new emphasis on anisotropy was motivated by recent field observations from the New England Damage Experiment (NEDE) (Martin et al., 2012; Martin and Boyd, 2012). A preliminary analysis of the fractures produced by chemical explosions in a Barre Vermont granite quarry shows that strong asymmetries in the fracture pattern may be attributed to a preferred orientation of the initial microfractures in the granite (called the rift). In order to more quantitatively model this pattern and the associated seismic radiation we have extended our damage model to allow an anisotropic distribution of initial damage. Finally, other aspects of the NEDE observations that directly support our numerical model include the observation of a strong second P wave pulse in the near-field and a dependence of the spatial extent of the fracture pattern and the strength of S waves on the loading rate (burn rate) of the explosive.

2. INTRODUCTION

A central challenge in the seismic monitoring of nuclear explosions is the discrimination between explosions and earthquakes. The problem is made difficult by the fact that seismic signals from underground explosions contain significant S wave energy. How much of this S energy is generated in the non-linear source regime and how much is due to mode conversion along the path has yet to be resolved. Understanding the mechanisms that generate S waves is especially important in recent attempts to identify small explosions using regional phases.

This study is aimed at understanding and numerically modeling the seismic radiation that is generated in the region of an explosive source that is dominated by the nucleation and growth of fractures, which we term the damage zone. Our approach has been to develop a fully dynamic micromechanical damage mechanics and build it into the dynamic finite element program ABAQUS. Our damage mechanics is unique in two important ways: 1) it is micromechanical in that it models the nucleation, growth, and interaction of individual fractures, and 2) it is valid at the extremely high loading rates found in the non-linear source regime of an explosion (or near the rupture front of an earthquake, or in rock beneath a meteorite impact).

A second part of our study has been to validate this damage mechanics model. We have shown in Bhat et al. [2012] that we are able to predict the failure strength of Pentelicon marble (from the Parthenon in Greece) over a range of loading rates that span 10 orders of magnitude extending to 10^4 sec^{-1} . We have generated fracture patterns in the laboratory by exploding nichrome wires in “candy glass” plates and measuring the resultant seismic radiation in the near field using laser vibrometers. We found that the dilatation associated with the fracture damage generated by the explosion makes a significant contribution to the radiated P waves (as originally predicted by Johnson and Sammis [2001]) and that a slight asymmetry in the pattern of long radial fractures produces S wave radiation. In order to use these laboratory experiments to test our damage mechanics model we had to measure the mechanical properties of candy glass. These include the elastic constants, the density, the critical stress intensity factor, and the initial damage (flaw size and density). The candy glass experiments are currently being prepared for publication [Mihaly et al., 2015].

A third part of our study has been to interpret the fracture patterns and seismic radiation produced by the New England Damage Experiment (NEDE), a suite of small chemical explosion in a granite quarry in Barre, New Hampshire. These carefully controlled field experiments have been a windfall for our project by providing data on the effect of loading rate on the size of the fracture pattern and resultant S wave radiation. They also provided evidence that the double P wave peak seen in the near-field laboratory and numerical simulations is also observed at the field scale. The observation that the subtle alignment of microfractures in the Barre granite (the rift) caused a large asymmetry in the fracture pattern and in the resultant seismic radiation has motivated us to spend the past year modifying our damage mechanics to allow an anisotropic distribution of initial fracture damage.

3. METHODS, ASSUMPTIONS, AND PROCEDURES

Our approach has been a combination of numerical modeling and laboratory studies using high-speed digital photography and laser vibrometers as high-frequency seismometers. We first discuss our approach to numerical modeling, and then the details of our laboratory experiments. Results of the modeling and experiments are presented in section 4.

3.1 Numerical Modeling – Dynamic Damage Mechanics

We used the micromechanical damage mechanics originally formulated by Ashby and Sammis [1990] and generalized by Deshpande and Evans [2008]. As illustrated in Fig. 1, frictional sliding on the optimally oriented initial flaws nucleates tensile wing-cracks which, at high stress, coalesce to pulverize the rock. If the initial fracture distribution is isotropic then there will always be optimally oriented starter flaws at any azimuth and the resultant damage pattern will have spherical symmetry.

We made further modifications, detailed in Bhat et al. [2012], to allow for a more generalized stress state and to incorporate an experimentally motivated new crack growth (damage evolution) law that is valid over a wide range of loading rates. This law is sensitive to both the crack tip stress field and its time derivative. Incorporating this feature produces strain-rate sensitivity in the constitutive response. Our fully dynamical damage mechanics was implemented as a user-defined subroutine in the ABAQUS dynamic finite element code. Bhat et al. [2012] validated the model by correctly predicting the observed stress-strain behavior of Pentelicon marble over a 10 order of magnitude range of loading rates and using it in first order simulations of an underground explosion and an earthquake.

3.2 Numerical Modeling – Anisotropic Initial Damage

A basic assumption of our damage mechanics is that the initial damage is isotropic. As illustrated in Fig. 1, this means that, independent of azimuth; the shock front always promotes sliding on the most optimally oriented flaws. However, microfractures typically have a preferred orientation (the rift), even in apparently isotropic rock like granite. Fig. 2 shows the velocity anisotropy caused by the rift in Barre granite from the quarry in which the NEDE field experiments were performed.

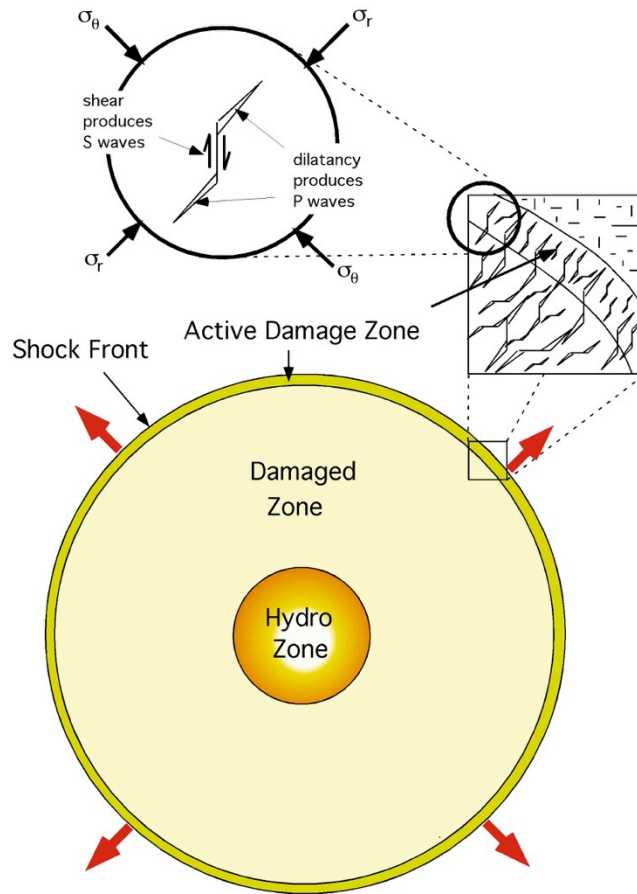


Figure 1. Isotropic damage generation in an explosion.

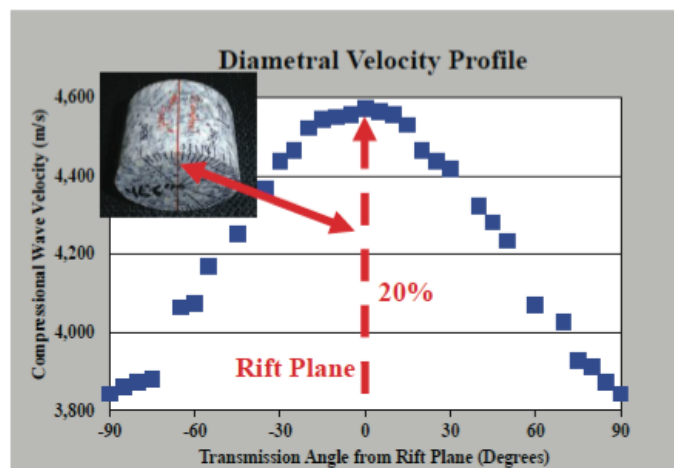


Figure 2. Velocity anisotropy in Barre granite indicates a fracture anisotropy with microfractures preferentially aligned in the “rift plane”. (From Martin and Boyd, 2012).

Figure 3 shows the damage pattern produced by a NEDE explosion. Note that the fracture damage extends vertically and horizontally following the rift plane. These directions are optimal

for damage creation during the first dilation phase of the pressure front when the hoop stress $\sigma_{\theta\theta}$ becomes tensile. Note also the slight enhancement of damage at an elevation of about 45° from the shot point. This is the optimal direction for the Ashby/Sammis shear mechanism as indicated.

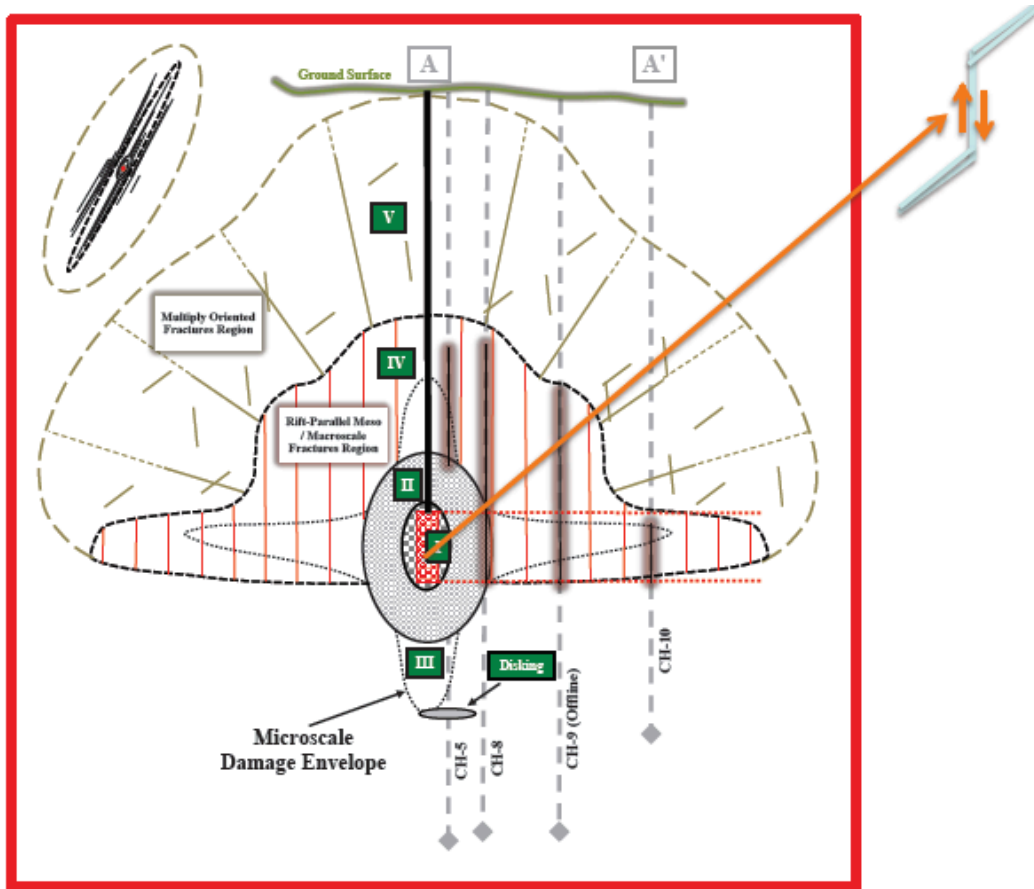


Figure 3. Damage pattern produced by a NEDE explosion (redrawn from Martin and Boyd, 2012).

Figure 4 shows the dynamic stress field in the near-field calculated by Johnson and Sammis (2001). Note that fracture damage occurs when the transverse stress $\sigma_{\theta\theta}$ becomes tensile. Our physical interpretation of this observed anisotropy in the fracture pattern is that microfractures in the rift plane extend preferentially during the time when the transverse hoop stress becomes tensile. A unique feature of our new dynamic damage mechanics is that it models crack growth in the tensile regime, which was not possible in the Johnson and Sammis (2001) simulations that used the Ashby and Sammis (1990) formulation, which was limited to compressional loading.

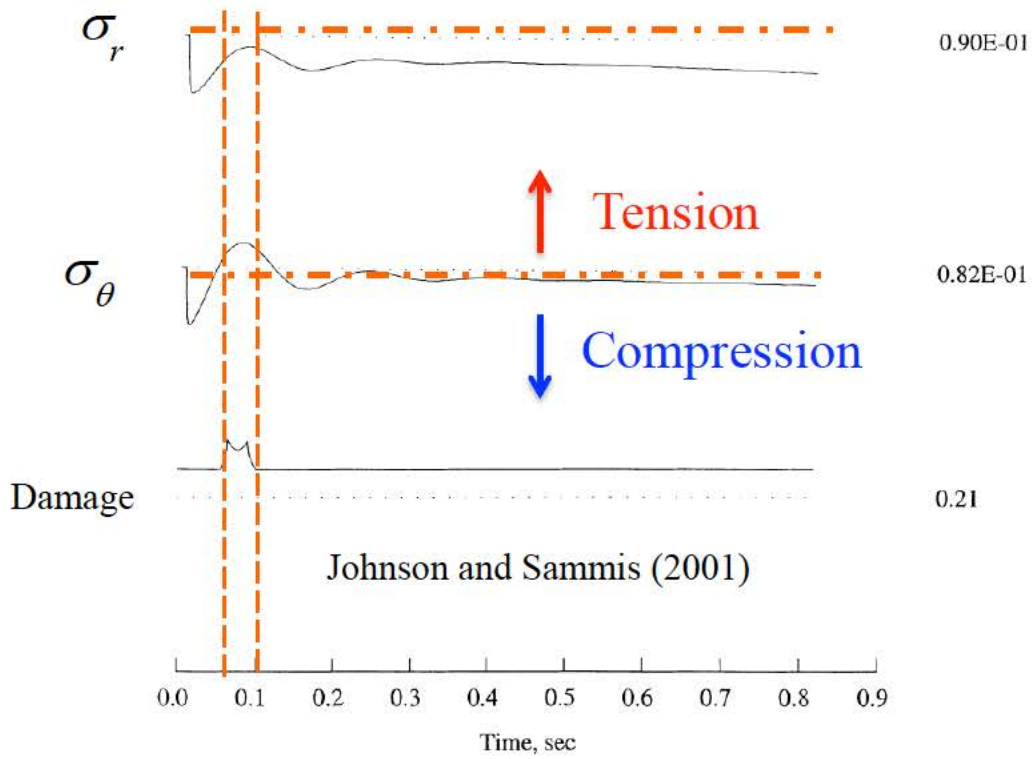


Figure 4. Dynamic stresses in the near-field of an explosion (redrawn from Johnson and Sammis, 2001).

When the initial fracture distribution is anisotropic, each azimuth has a different angle Ψ between the fractures and the outward normal explosive stress as shown in Figure 5. We model this by dividing the region into azimuthal wedges, each of which has a different angle Ψ . The rift direction has the highest initial damage state. It is not activated in compressive sliding but is activated when the hoop stresses turn tensile (as in Fig. 4) to produce the extensive damage observed in the rift direction in the NEDE field experiments. Since the initial damage is defined as $D_0 = \frac{4}{3} \pi N_V (\alpha a)^3$ and $\alpha = \cos \Psi$, we can express this azimuthal variation in Ψ as an azimuthal variation in D_0 as shown in Fig. 6. N_V is the initial flaw density and a is the flaw size.



Figure 5. Explosion in granite that has a preferred fracture orientation (rift plane). *In this case, the angle Ψ between the largest principal compressive stress (radial) and the rift plane varies as indicated.*

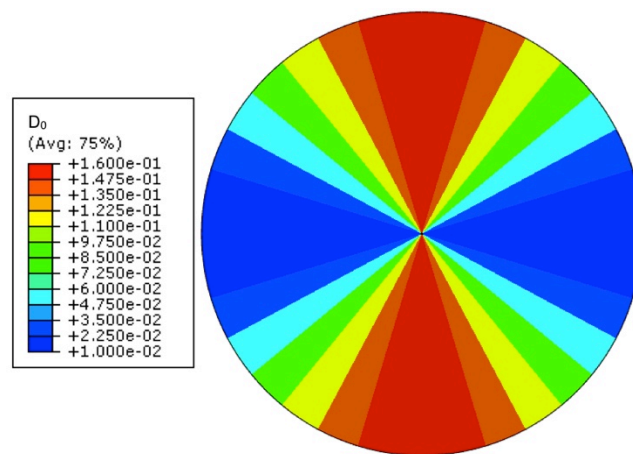


Figure 6. The initial damage state (D_0) of the model used to study an anisotropic solid.

3.3 Laboratory Experiments – Explosions in Candy-Glass Samples

Our first attempts to generate fracture patterns in the laboratory used hypervelocity impacts of mm size nylon projectiles on 6" x 6" x 1/2" plates of Homalite (a photoelastic polymer). The term "hypervelocity" indicates that the projectile is traveling faster than the P wave velocity in the target. The result is a shock-like explosion with no spalling. We performed these experiments using the two-stage light gas gun in Professor Rosakis' high-speed photography laboratory at Caltech. This facility was originally built to study micrometeorite impacts in order to design protective shields for space vehicles.

To our surprise, these experiments produced strong S waves. We were surprised because a prior study by Johnson and Sammis [2001] concluded that an asymmetry caused by either prestress or prior damage is required to generate S waves. Neither asymmetry was present in these lab experiments. Rather, the cylindrical symmetry was broken in this case by the asymmetric growth of long radial fractures. Tensile opening of these fractures resulted in the radiation of S waves. Numerical simulations presented in the next section support this interpretation.

These hypervelocity impact experiments were not entirely satisfactory for two reasons: 1) we cannot be sure that there is no out-of-plane deformation. Bending would produce tensile stress enhancing crack growth, and 2) the impact experiments are done in an evacuated chamber, making asymmetric loading and the use of laser velocimeters to measure particle motion in the elastic waves experimentally difficult.

Ideally, we would like to use a point explosion to produce the fracture pattern so that we can perform the experiments in our loading frame while instrumenting the sample with laser velocimeters to record particle velocities during the passage of the elastic waves. We first attempted this by inserting a very thin nichrome wire through a small hole in the center of the Homalite (polymer) plates. The wire was exploded using a high-voltage pulse from a bank of capacitors (which also triggered the high-speed cameras. The experimental set-up is shown in Fig. 7. The alligator clips that attach the capacitor bank to the nichrome wire indicate the location of the explosion. Also shown are the positions of the 3 laser reflectors (A, B, and C) used to measure the particle velocity. Site (A) is on the sample surface 10 mm from the explosion, site (B) is on the sample surface 35 mm from the explosion and site (C) is on the edge of the sample. Sites (A), (B), and (C) are essentially ultra-high-frequency single-component velocity seismometers. Sensors A and C measure radial motion while sensor B measures transverse motion.

This is the same technique we used to nucleate frictional sliding on a stressed surface (the explosion instantaneously relieves the normal stress on a small nucleating patch). The problem was that the explosion did not generate enough energy to produce a fracture pattern in the Homalite sample. We have solved this problem by switching from Homalite to "candy-glass" (also known as "break-away glass"). This is the material used in movie stunts that involve breaking glass without injuring the stunt men, e.g., in bar-fights. Its safety comes from its very low fracture toughness, which we have measured to be a factor of 67 times lower than that in either Homalite or glass. Consequently, our exploding wires produce sufficient energy to generate extensive fracture patterns.

The waveform of the elastic waves was recorded using laser velocimeters. These instruments bounce a laser beam off a mm size corner reflector to measure one component of its velocity. Each reflector thus acts as a broad-band seismometer.

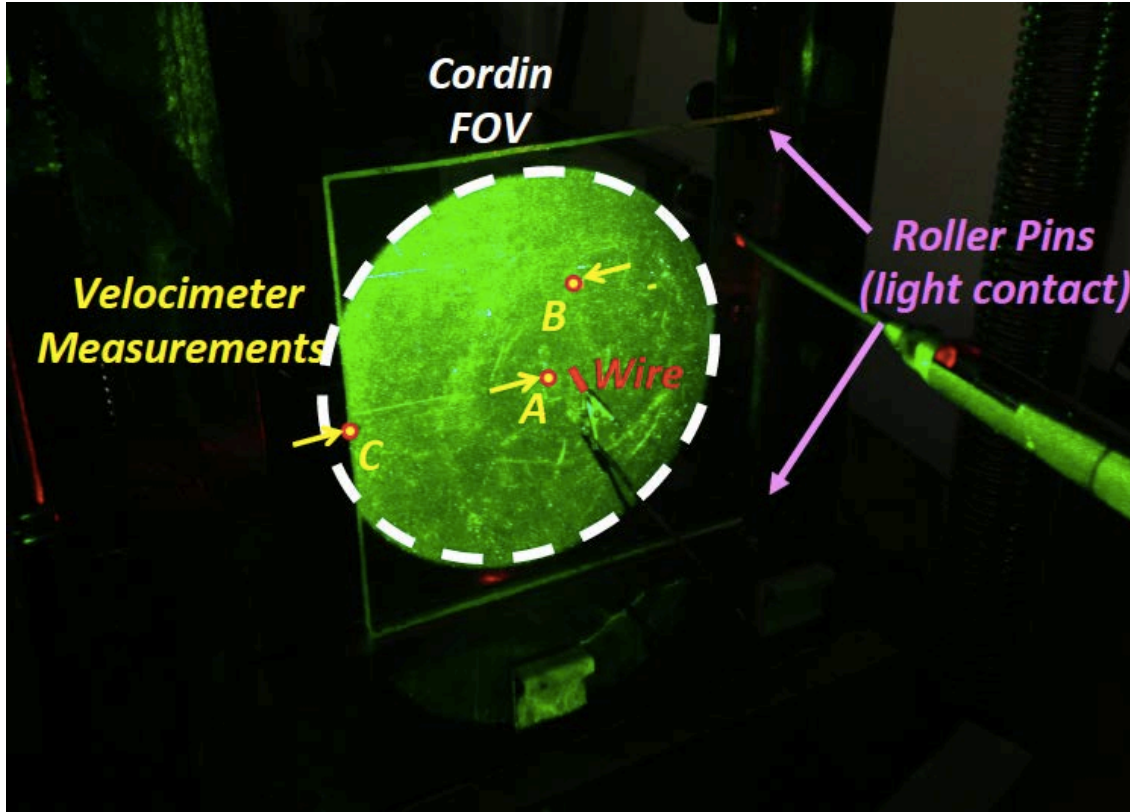


Figure 7. Experimental configuration used to produce fracture patterns in candy-glass.

4. RESULTS AND DISCUSSION

4.1 Experimental Results - Candy-Glass Plates

Figures 8 through 11 show selected high-speed camera images before, during and after an explosion. Figure 12 shows a post-test image of the sample. Next to it is the fracture pattern produced by a nuclear explosion as revealed by fracture mapping in mine shafts and boreholes. Note that the candy glass explosion produces the main morphological characteristics of the nuclear explosion: the extensive fragmentation close to the source and the longer isolated radial fractures.

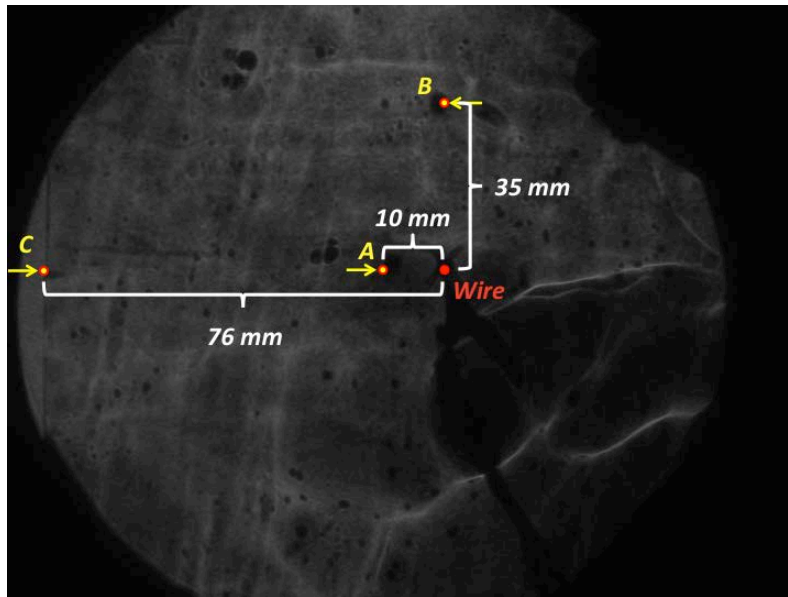


Figure 8. Photo of a sample before the explosion showing placement of the laser sensors. *The illuminated circle is the field of view of the high-speed Cordin cameras as indicated by the white dashed circle in Fig. 7 above. This photo was taken using Polaroid filters that reveal small-scale heterogeneity in the sample.*

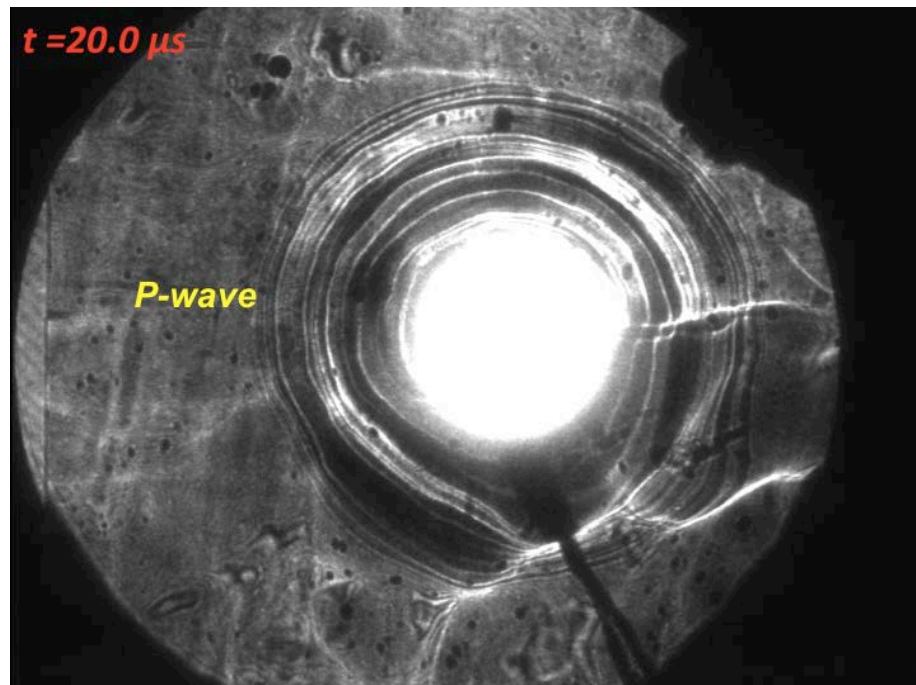


Figure 9. Image of the sample 20.0 μs after the explosion. *The flash from the explosion is evident. Candy-glass has a sufficiently large photoelastic constant to reveal the P wave, which has moved 40 mm in 20 μs , or 2000 m/s, which is slightly below the average P wave velocity, which we measured ultrasonically to be 2162 m/s.*

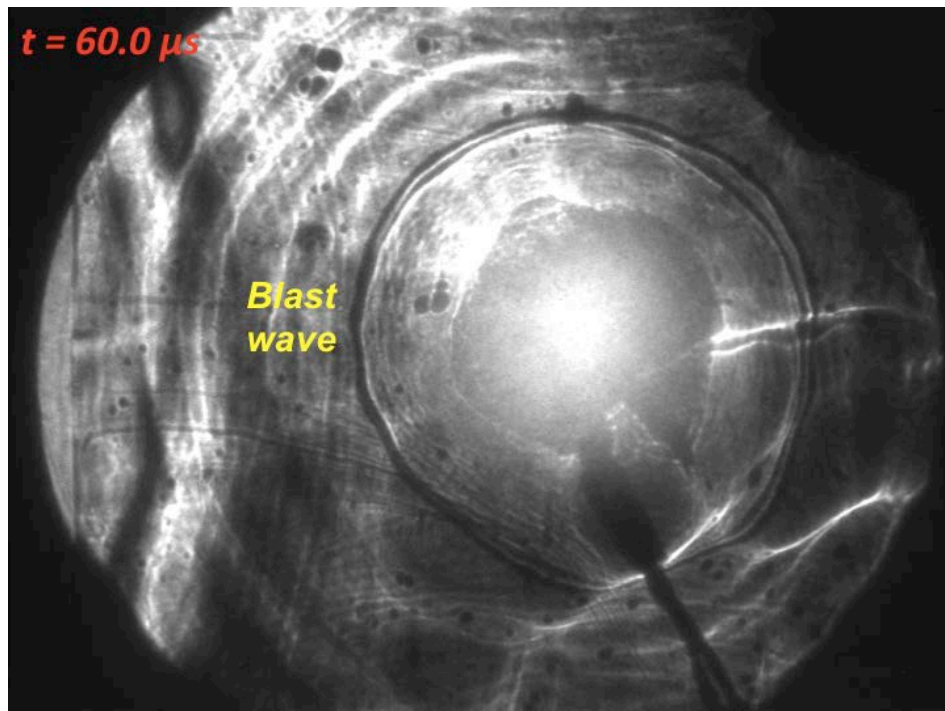


Figure 10. Image of the sample 60.0 μs after the explosion. *The flash from the explosion is still visible as is a debris cloud that, unfortunately, hides the emerging fracture pattern. The thin dark circle is the blast wave that is traveling at the speed of sound in air.*

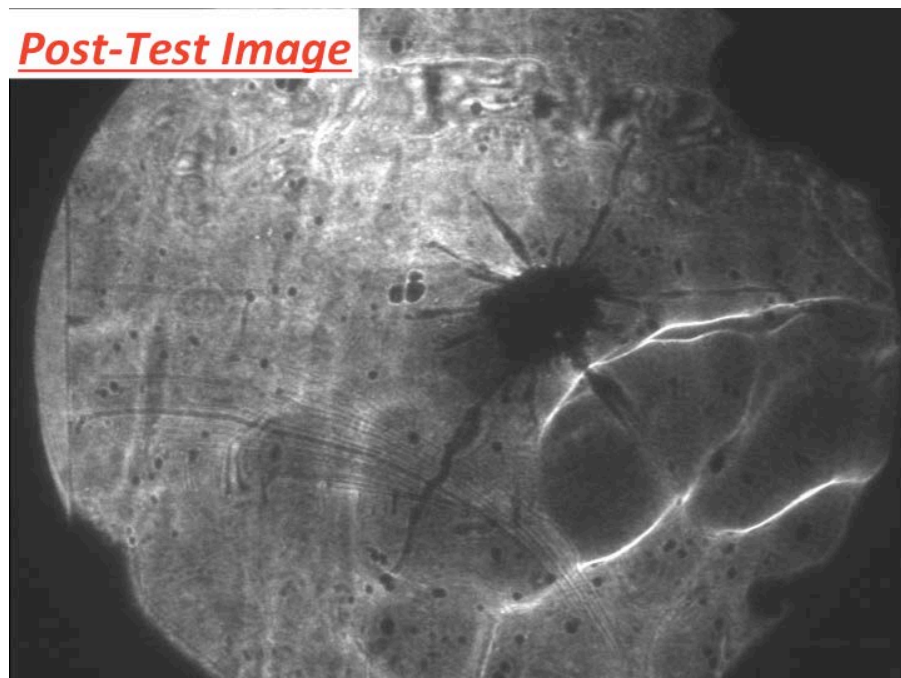


Figure 11. Image of the sample at the end of the experiment showing the fracture pattern.

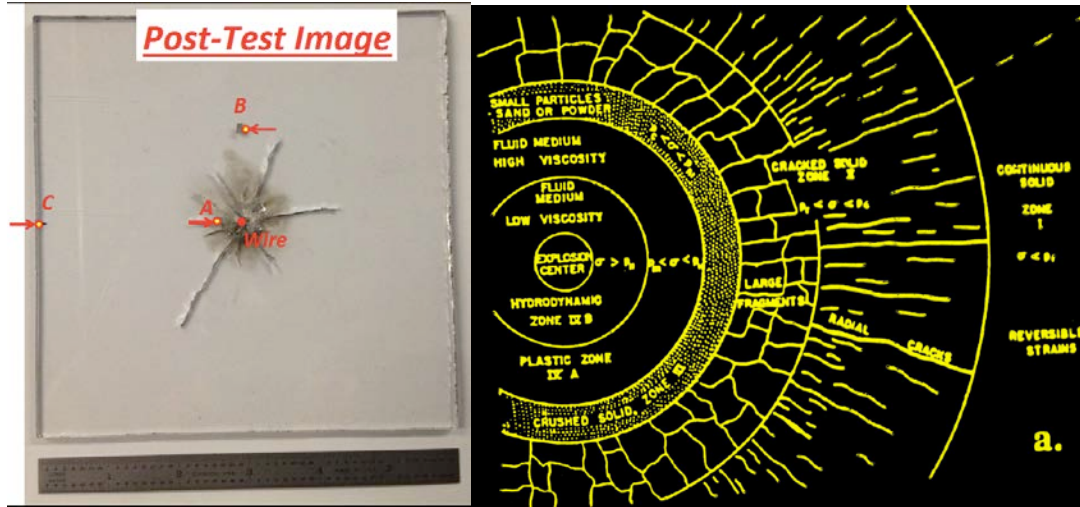


Figure 12. Comparison of the experimental fracture pattern with that produced by an underground nuclear explosion. Both patterns are characterized by radial and circumferential cracking close to the explosion and a set of radial cracks that extend well beyond the circumferential cracks. Note that reflector (A) lies within the pattern of circumferential fractures.

Figures 13 and 14 show the signals from the three laser velocimeters in experiments #1 and #2 respectively. The red trace from the sensor at location (A) shows a double peak structure in both experiments. Our interpretation is that the first peak is the P wave arrival while the second peak is the arrival of the damage front, which Johnson and Sammis [2001] showed travels at a velocity between V_P and V_S .

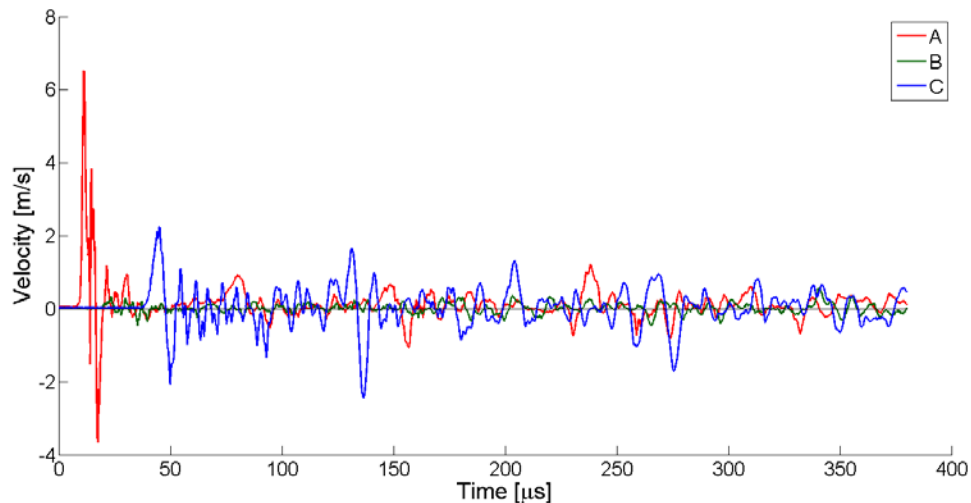


Figure 13. Recordings of the x component of velocity from experiment #1 recorded at the three stations indicated in Fig. 2. Stations A and C recorded radial velocity. Station B recorded transverse velocity (x is in the θ direction).

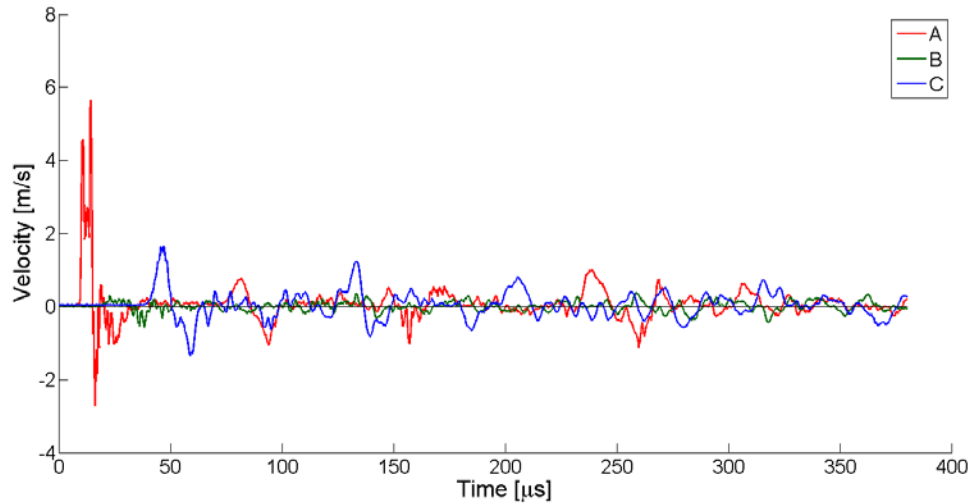


Figure 14. Recordings of the x component of velocity from experiment #2, which used the same station configuration as experiment #1 as indicated in Fig. 2. Note the repeatability of the experiment. Also note that both records have a large initial double peak at station A.

Figure 15 shows the travel paths of the arrivals on the travel time curves in Figures 16 and 17.

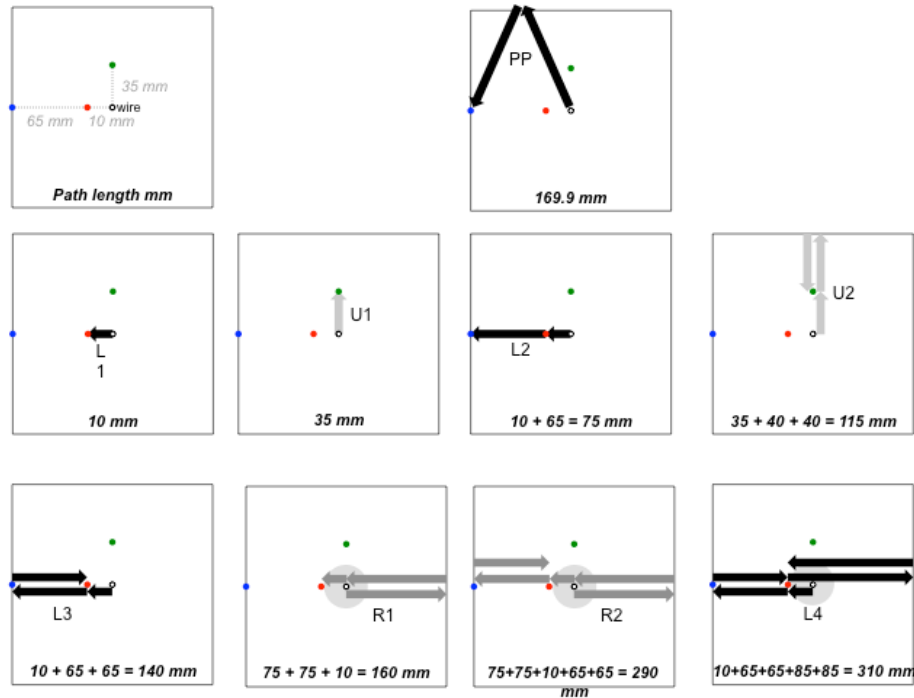


Figure 15. Travel paths for the arrivals plotted on travel time curves in Figs. 16 and 17. Note that R1, R2, and R4 pass through the damage zone producing delayed arrivals. The slowness through the damage zone can be used to calculate the total damage.

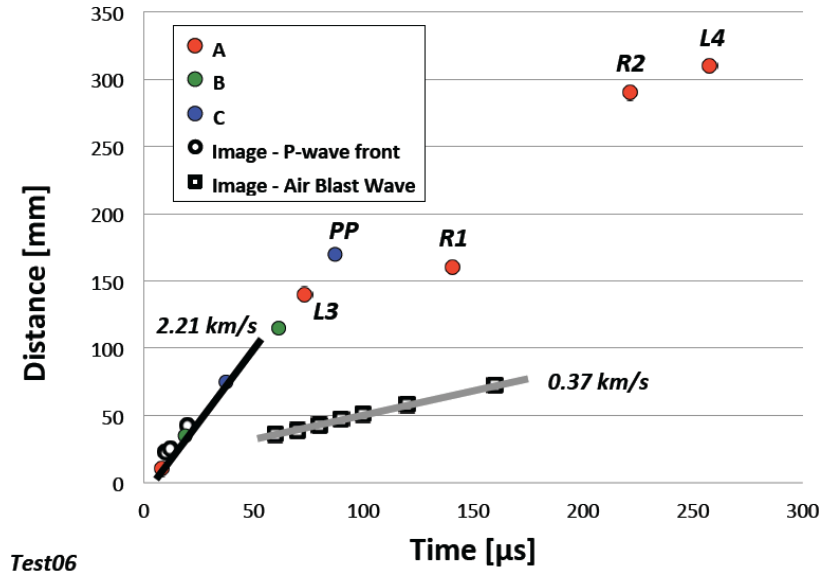


Figure 16. Travel time curves for experiment #1 (*seismograms in Fig. 7*). Note that the *P* wave and air blast wave are easily identified. Arrivals *R1*, *R2*, and *R4* are delayed by passage through the damage zone. Note also that the velocities measured from the high-speed images are consistent with those from the vibrometer stations.

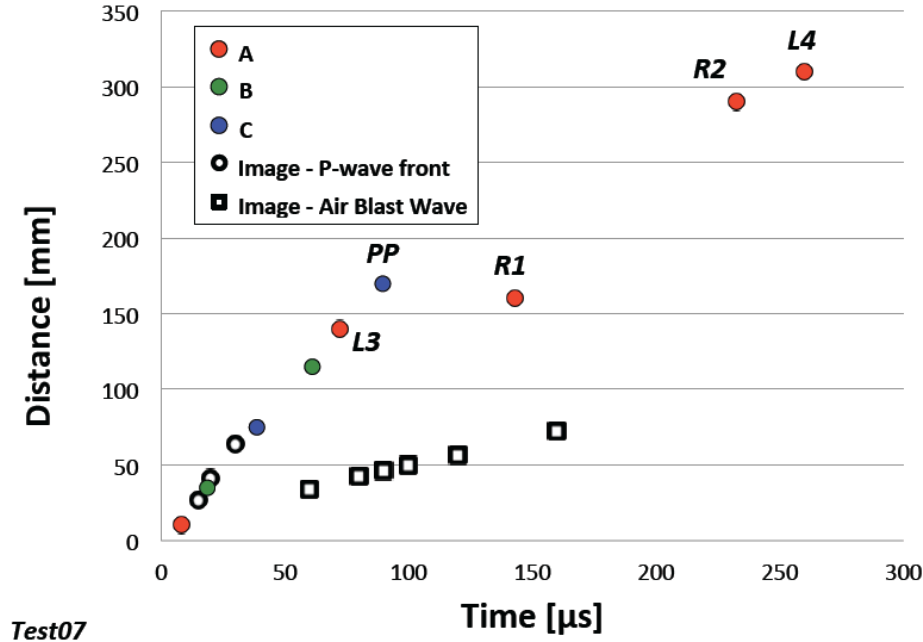


Figure 17. Travel time curves for experiment #2. Note the consistency with experiment #1 in Fig. 16.

The time delay of 55 μsec across the 10 mm damage zone experienced by R1, R2, and L4 can be used to quantify the damage in the heavily damaged zone near the explosion. This delay corresponds to a ratio of damaged to undamaged velocities of $v_d/v = 0.144$, which, using O'Connell and Budianski (1974), corresponds to $N_v \langle \alpha^3 \rangle = 0.55$, which in turn corresponds to a damage of $D = \frac{4}{3} \pi N \langle \alpha^3 \rangle = \frac{4}{3} \pi 0.55 = 2.3$. Since we stop damage accumulation in our simulations at $D=1$, we underestimate the effects of damage in the simulations. How to model post-failure damage accumulation and the associated deformation remains a major unsolved problem in theoretical mechanics.

4.2 Measurements of the Mechanical Properties of Candy-Glass

The primary objective of the experiments in candy-glass is to validate our high-speed micromechanical damage mechanics by directly modeling the fracture patterns and associated seismic radiation. Our dynamic damage mechanics model requires the following inputs: Isotropic elastic velocities V_P , V_S and the density ρ (or two equivalent isotropic elastic moduli and the density), the critical stress intensity factor for mode I loading K_{IC} (or equivalently, the fracture toughness), and the initial damage (or equivalently the size and density of initial flaws). The “candy glass” plates used in these experiments is not the simple sugar glass originally used by the movie industry, but a proprietary polymer. Since the mechanical properties of this material were unknown when we began our study, we had to measure those mechanical properties required by our damage mechanics model.

In order to determine the elastic constants, we sent a sample to Peter Boyd at New England Research who measured the density and the P and S wave velocities at the four locations indicated in Fig. 18. V_{S1} and V_{S2} are orthogonal S wave polarizations. Note that there is a slight elastic anisotropy in the sample. Note also that there is an 0.4 mm, or about 10% variation in sample thickness.

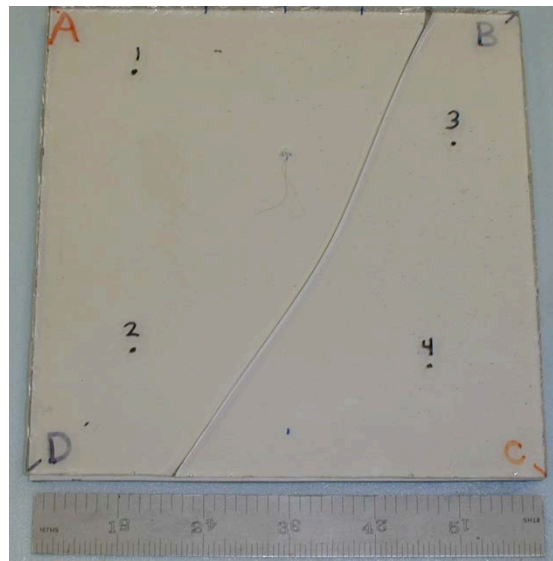


Figure 18. Locations of the ultrasonic measurements of V_P and V_S in a candy-glass plate.

Table 1. Elastic properties of candy-glass measured at New England Research.

Sample	Thickness (mm)	Density (gm/cm ³)	V _p (m/s)	V _{s1} (m/s)	V _{s2} (m/s)	Young's (GPa)	Poisson
1	4.80	1.041	2173	1127	1075	3.35	0.327
2	4.78	1.041	2156	1113	1057	3.26	0.330
3	4.47	1.041	2179	1110	1048	3.24	0.338
4	4.47	1.041	2138	1115	1024	3.17	0.333

Average properties are:

$$V_p = 2162 \pm 18 \text{ m/s}$$

$$V_{s1} = 1116 \pm 7 \text{ m/s}$$

$$V_{s2} = 1051 \pm 21 \text{ m/s}$$

$$\text{Young's Modulus} = 3.26 \pm 0.07 \text{ GPa}$$

$$\text{Poisson's Ratio} = 0.332 \pm 0.005$$

The other mechanical parameter we need for the numerical modeling is the critical stress intensity factor K_{IC} . We measured K_{IC} using four-point bending tests as illustrated in Fig. 12. Results are summarized in Tables 1 and 2.

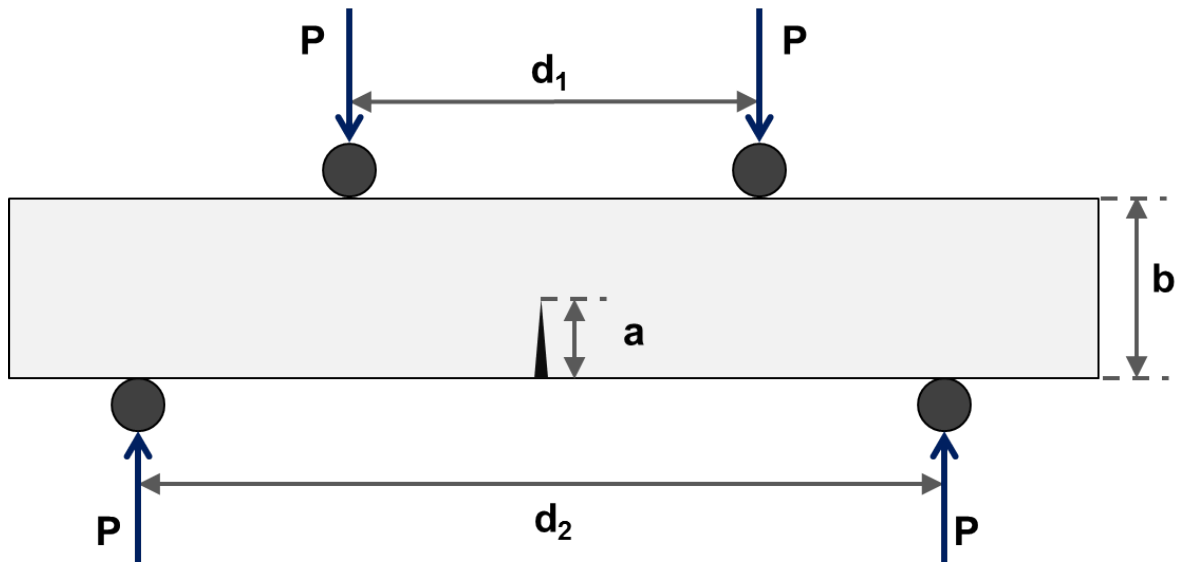


Figure 19. Four point bending geometry used to measure the critical stress intensity factor K_{IC} in candy glass.

Table 2. Specimen dimensions for the five test specimens

<i>Length</i>	63.9
<i>Thickness</i>	4.6
<i>b</i>	18.3
<i>d₁</i>	25.4
<i>d₂</i>	37.3

Table 3. Test data and measured values of K_{IC} for the five test specimens.

	Crack length <i>a</i> [mm]	<i>a/b</i>	<i>P_{fail}</i> [N]	K_{IC} [Pa*m ^{1/2}]
<i>Specimen 1</i>	11.9	0.650	13.52	32,885
<i>Specimen 2</i>	11.1	0.606	12.59	25,297
<i>Specimen 3</i>	5.4	0.294	22.03	16,384
<i>Specimen 4</i>	4.8	0.265	20.86	15,116
<i>Specimen 5</i>	6.5	0.353	16.97	15,300

Compare $K_{IC} = 0.015 \text{ MPa}\cdot\text{m}^{1/2}$ measure here in candy glass with $K_{IC} = 1 \text{ MPa}\cdot\text{m}^{1/2}$ typical of glass (and most oxides and silicates). The fact that the fracture toughness of candy glass is a factor of 67 times smaller explains why candy glass fractures so easily – in movies and in our experiments.

We also measured the initial flaw size and density in candy-glass by running a series of uniaxial compression tests on small prisms. The flaw size *a* was determined by the initiation of damage (first non-linearity in the stress-strain curve) using the expression (from Ashby and Sammis, 1990)

$$\sigma_1^* = \frac{\sqrt{3}}{(1 + \mu)^{1/2}} \frac{K_{IC}}{\mu \sqrt{\pi a}}$$

where σ_1^* is the stress at which nonlinearity is first observed, $\mu = 0.6$ is the coefficient of friction, and K_{IC} is the critical stress intensity factor (which we previously measured to be $K_{IC} = 1.56 \times 10^4 \text{ Pa m}^{1/2}$ in candy-glass).

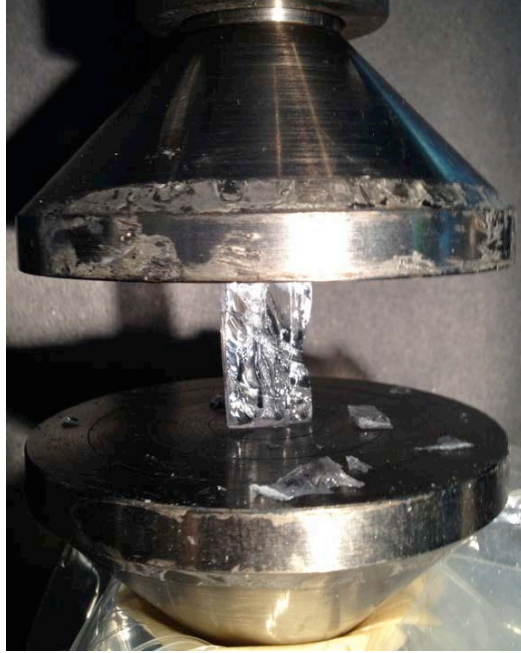


Figure 20. Experimental geometry used to measure the uniaxial strength of candy glass.

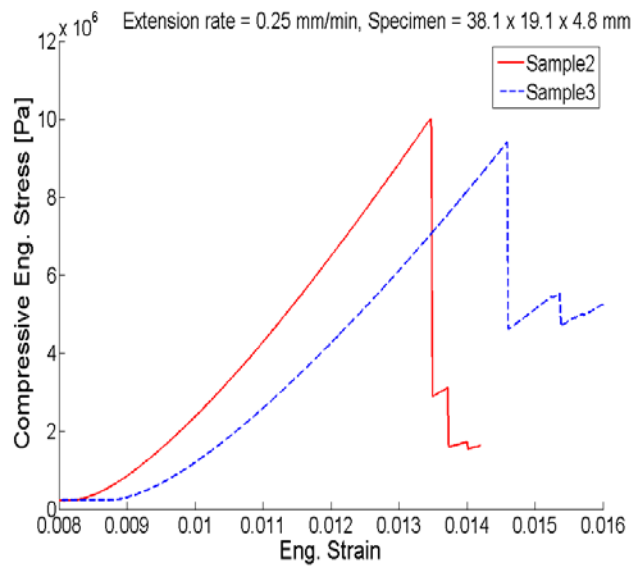


Figure 21. Uniaxial stress-strain curves for candy glass used to determine a and D_0 as described in the text.

Note that the stress strain curve is linear up to the failure stress in Fig. 21. This implies that the samples fail as soon as damage nucleates, which implies a relatively high initial flaw density. The above equation gives $a = 8.2$ microns.

Having determined the initial flaw size a , we found the initial damage $D_0 = \frac{4}{3}\pi N_V (\alpha a)^3$ that gives the observed failure stress in Fig. 21, which turns out to be $D_0 = 0.13$. D_0 and a then give the initial flaw density $N_V = 1.58 \times 10^{14}$ flaws/m³.

4.3. Numerical Simulations of Explosions

Figure 22 shows a direct simulation of experiment #2 using our fully dynamic ABAQUS finite element code. Note that our simulations produce a double peak, although not quite as large as in the experiment. This second peak is due to dilatation caused by the damage, which follows the first peak due to the explosion itself. The reason it is smaller may be due to the fact that we stop our simulation when $D = 1$. The analysis of the travel time curves above indicated that $D = 2.3$ in the highly damaged part of the fracture pattern. The dilatation associated with this post failure damage may produce the larger second peak in the experiment.

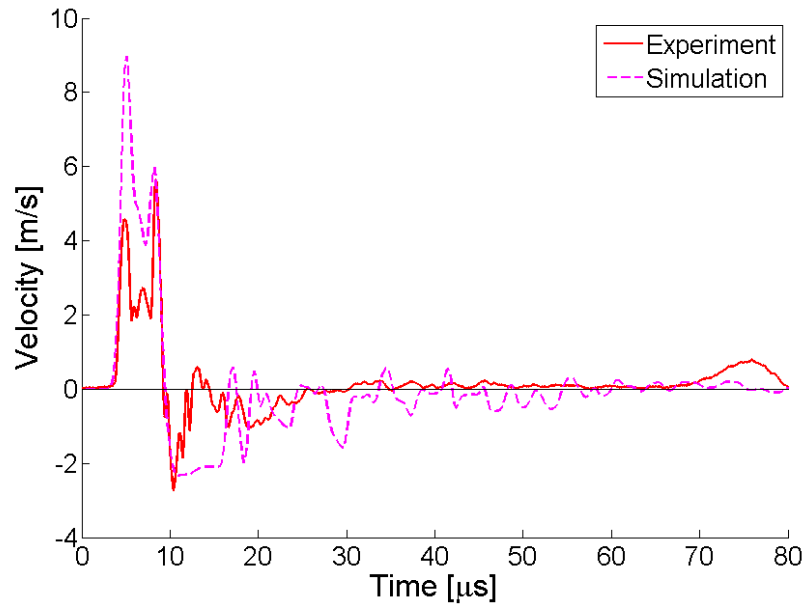


Figure 22. Comparison of the simulated and measured velocity at sensor A in experiment #2. Note that the simulation also produces a double peak.

In Figure 23 we have repeated the simulation in Fig. 22 except that we increased the critical stress intensity factor to a level where no damage is created by the explosion. The lack of a second pulse in this simulation confirms that the source of the second peak in Fig. 22 is the dilatation associated with fracture damage.

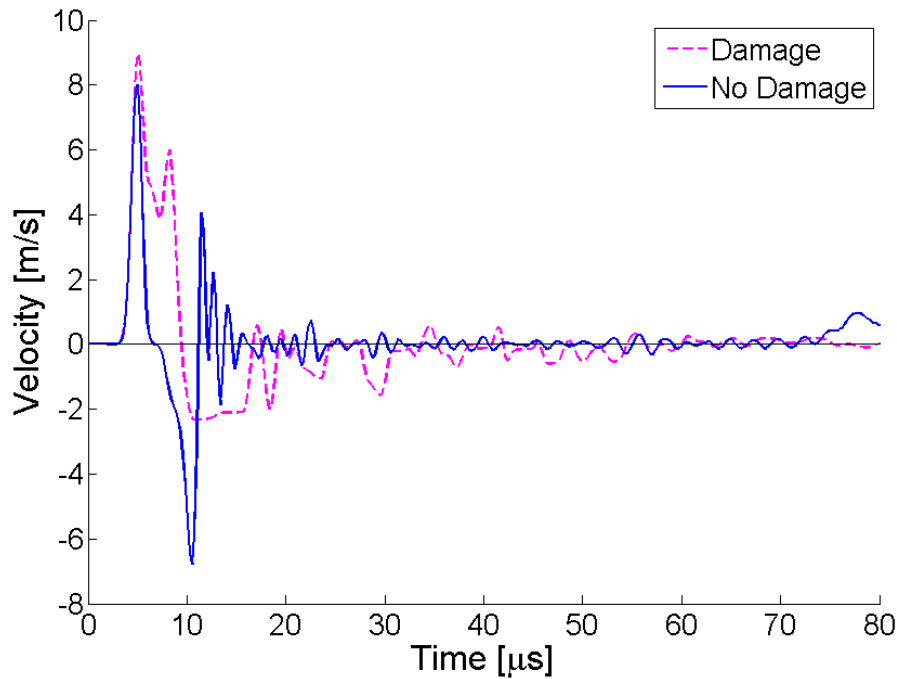


Figure 23. An identical simulation to that in Fig. 22 except that the critical stress intensity factor has been increased to the point where the explosion does no additional damage. *The lack of a double peak supports the hypothesis that it is produced by the damage.*

Figure 24 shows a radial velocity seismogram 15 meters from an explosion in the NEDE experiment (New England Research and Weston Geophysical) in a Barre Granite quarry. Note this field experiment also produced a strong double peak.

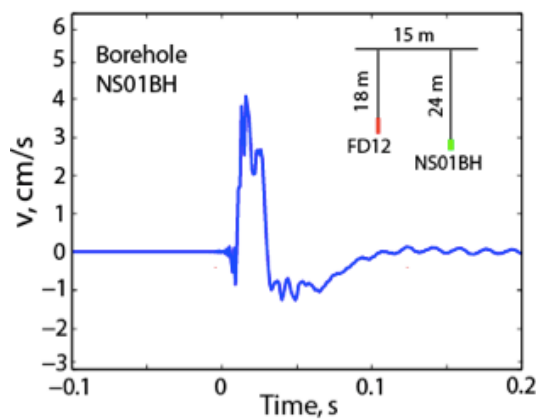


Figure 24. Radial velocity trace from a borehole seismometer 15 m from the NEDE chemical explosion in a Bare Granite quarry conducted by Weston Geophysical and New England Research. *(Courtesy of Anastasia Stroujkova, Weston Geophysical).*

Figure 25 shows the simulation of experiment #2 emphasizing the S arrival on the transverse sensor B. A similar weak S was observed on sensor B in the experiment.

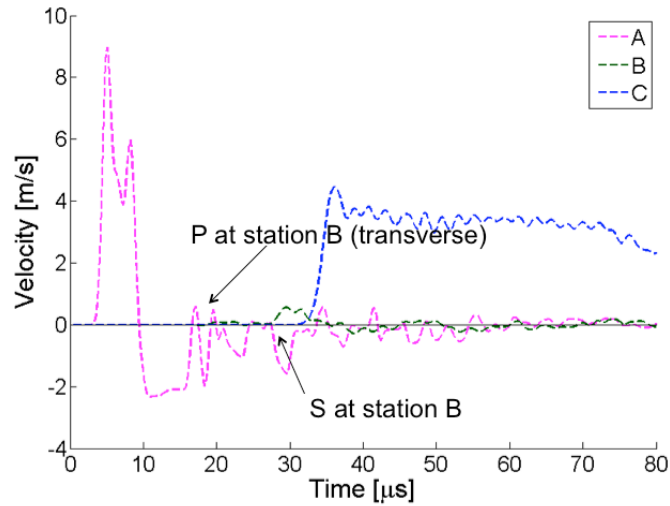


Figure 25. Simulation of the velocity traces in experiment #2. Note the weak arrival of P on the transverse sensor B (probably a Poisson effect) and the stronger arrival of S.

4.4. Effect of Burn-Rate (Loading-Rate) on the Damage Pattern

Figure 26 shows numerical simulations of point explosions in candy glass plates using our new dynamic damage mechanics model.

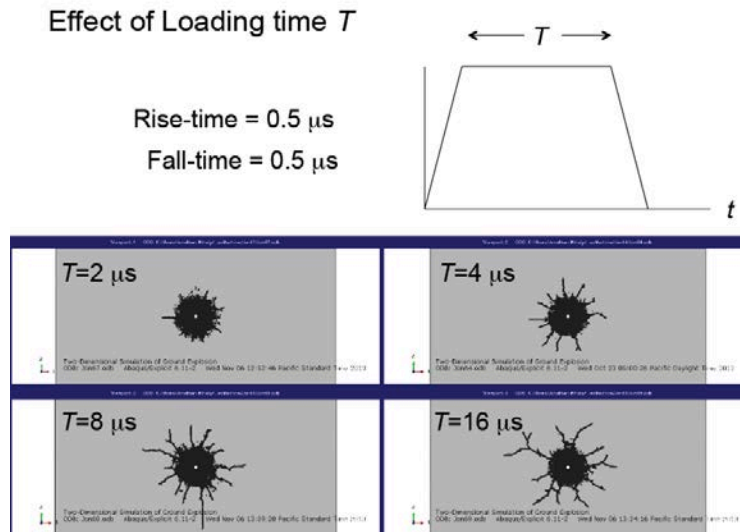


Figure 26. Numerical simulations of point explosions in candy-glass plates showing the effect of the duration of loading T.

Note that the spatial extent of the damage is controlled by the duration of the explosion. Longer loading times produce more extensive radial fracturing (and larger S waves). This effect was observed in the first set of NEDE experiments where the slower burning black powder explosion produced more radial cracking and larger S waves than the faster burning ANFO and COMP-B explosions.

4.5. Modeling an Anisotropic Initial Flaw Distribution

The results of a 2D simulation of an explosion in the anisotropic medium shown in Figs. 5 and 6 are shown in Figs. 27 and 28. Note the extension of damage in the rift direction in Fig. 27 and the S wave radiation pattern in Fig. 28, which was produced by sliding on the initial fractures in the rift plane.

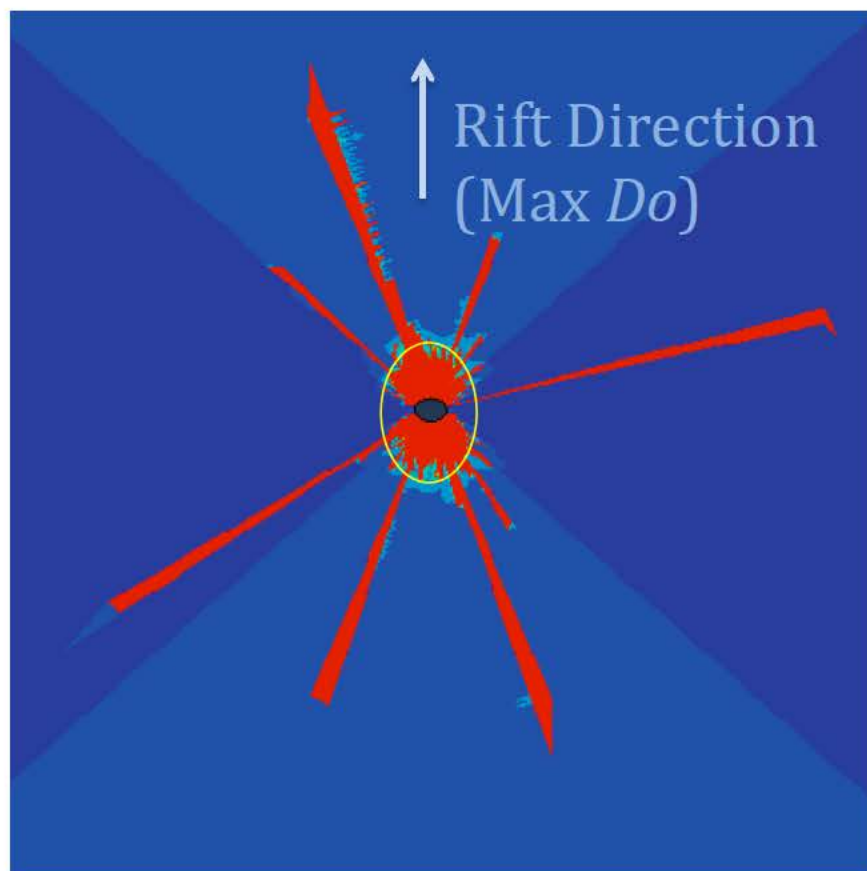


Figure 27. Numerical simulations of a point explosion in an anisotropic medium where the initial fractures have a preferential alignment in the rift direction. Note that the pulverized rock (indicated by the yellow ellipse) is extended in the rift direction as observed in the NEDE experiments. We are working to understand the seemingly random orientation of the long radial fractures.

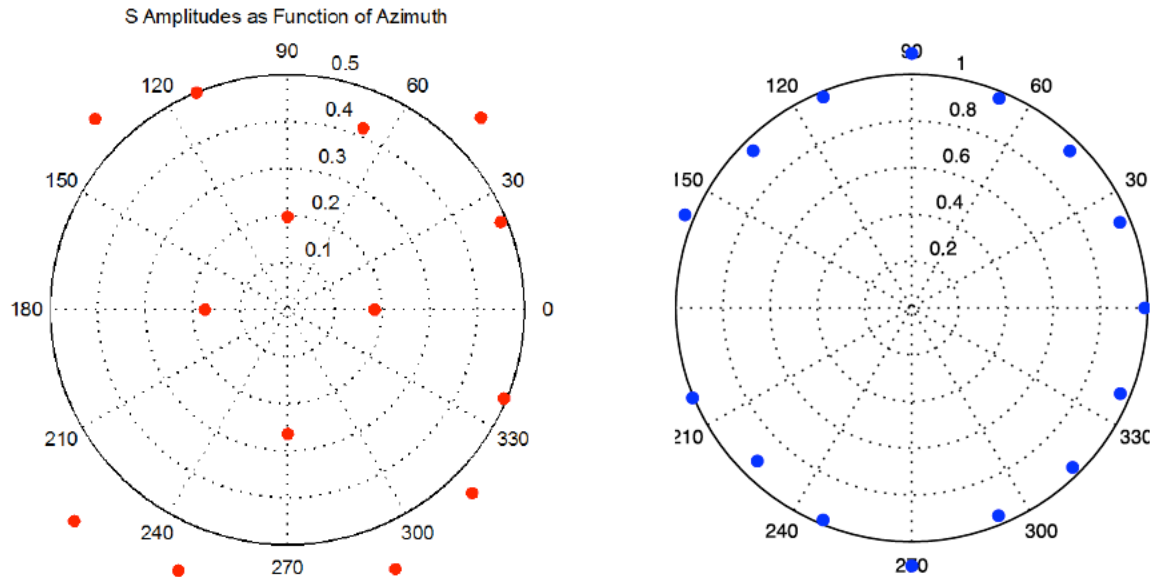


Figure 28. Numerical simulation of the P and S wave radiation from a point explosion in an anisotropic medium where the initial fractures have a preferential alignment in the rift direction, which is at 45° in this case. *Note the strong S wave pattern produced by sliding on the initial cracks in the rift plane.*

5. CONCLUSIONS

Based on the numerical and experimental studies presented above, we draw the following conclusions:

1. Any asymmetry in the generation of fracture damage produces S wave radiation.
2. A preferred orientation of microfractures (rift) in crystalline rocks can produce a strong asymmetry in damage generation leading to S wave radiation.
3. Since most preexisting micro and macrofractures are vertically oriented, this may explain the formation of chimney structures above explosions rather than the broad hemispherical or conical fracture pattern toward the surface predicted by isotropic damage models.
4. The dilatation associated with damage at the pressure front should produce a second P pulse that is observable in the near field.
5. The burn-rate of an explosion has a strong influence on the extent of radial fracturing. For explosions having the same energy, slower burn-rates produce larger fracture patterns and more S wave energy than do faster burn-rates.

6. RECOMMENDATIONS

We recommend that the numerical simulations now be extended to 3D. The main purpose of the 2D simulations was to test the damage mechanics against the 2D candy-glass experiments and to begin to understand the effects of an anisotropic initial fracture distribution on the final fracture pattern and accompanying seismic radiation. The reason to now extend the numerical

modeling to 3D is that we wish to calculate moment tensors in the far-field for direct comparison with field observations. It has been widely reported that the point source representation of many explosions has a compensated linear vector dipole (CLVD) component. Although this is generally ascribed to an interaction with the free surface, anisotropic fracturing may also contribute. In order to explore the generation of CLVD and other non-spherical radiation from the source, we need to go to 3D. The ultimate goal is to map structure in the damage regime and the interaction with the free surface into contributions to the moment tensor that are readily measured using standard seismology.

REFERENCES

- Ashby, M. F. and C. G. Sammis, 1990, The damage mechanics of brittle solids in compression, *Pure Appl. Geophys.*, 133(3), pp. 489-521.
- Bhat, H. S., A. J. Rosakis, and C. G. Sammis, 2012, A micromechanics based constitutive model for brittle failure at high strain rates, *J. Appl. Mech.*, 79(3), 031016, doi:10.1115/1.4005897.
- Deshpande, V. S. and A. G. Evans, 2008, Inelastic deformation and energy dissipation in ceramics: A mechanism-based constitutive model, *J. Mech. Phys. Solids*, 56(10), pp. 3077-3100.
- Johnson, L. R. and C. G. Sammis, 2001, Effects of rock damage on seismic waves generated by explosions, *PAGEOPH*, 158, pp. 1869-1908.
- Martin, R. J. and P. J. Boyd, 2012, Characterization of Damage In Anisotropic Rock Due to Buried Explosions, In *46th US Rock Mechanics/Geomechanics Symposium*, American Rock Mechanics Association.
- Martin, R, P. Boyd, A. Stroujkova, M. Leidig, J. Lewkowicz, and J. Bonner, 2012, Anisotropy of the Barre Granite in the Vicinity of the NEDE, MRR Report.
- Mihaly, J.M., C. G. Sammis, A. J. Rosakis, and H. S. Bhat, 2015, Elastic Radiation Generated by a Point Explosion in Breakaway-Glass Plates, in preparation for submission to *Bull. Seism. Soc. Am.*
- O'Connell, R. J. and B. Budianski, 1974, Seismic velocities in dry and saturated cracked solids, *J. Geophys. Res.*, 79, pp. 5412-5426.

DISTRIBUTION LIST

DTIC/OCP

8725 John J. Kingman Rd, Suite 0944
Ft Belvoir, VA 22060-6218

1 cy

AFRL/RVIL

Kirtland AFB, NM 87117-5776

2 cys

Official Record Copy

AFRL/RVBYE/Dr. Robert Raistrick

1 cy